Multi-objective optimization for 3D printed origami crash box cell based on artificial neural networks and NSGA-II

Jiahao Li*, Minjie Qu, Zhiyu Jiang

School of Textile and Material Engineering, Dalian Polytechnic University, Dalian, 116034, China
*Corresponding author

Keyword: 3D-printing; Nylon composites; Carbon fiber; Origami crash box; ANN; NSGAII

Abstract: Composite structures are increasingly used in the automotive industry due to their lightweight and specific energy absorption capabilities, while 3D printing is also widely used in industry because of their high efficiency and high precision. Recently, the Origami crash box (OCB) has been proposed as an energy absorber for automobiles because of their low initial peak load and high average load. Experiments and theory have shown that the energy-absorbing effect of OCB will change significantly with the change in size. Since OCB is composed of multiple OCB cells, therefore, it is necessary to develop a model that can predict the energy absorption effect according to scale change of OCB cell. And this model is utilized to optimize the size to maximize its energy absorption capability while reducing the initial peak force. This paper explores the energy absorption effect of 3D printed OCB, which is made of carbon fiber-reinforced nylon in the same wight and thickness with a stable surface area of $14400mm^2$. The Artificial Neural Network (ANN) model which used Mean Squared Error (MSE) to measure its accuracy is established to predict high non-linear behavior of OCB cell at different size. And then the Non-dominated Sorting Genetic Algorithm (NSGA-II) in which initial Peak Crush Force (PCF) and Energy Absorption (EA) are used as optimization metrics, is applied to complete the multi-objective optimization. The utilized ANN model precisely predicts the variation of load capability with displacement in different size of OCB cell with an MSE as 0.046kN？energy error as 5.97J and PCF error as 0.17kN. A configuration of OCB is generated by NSGA-II shows superior performance than standard OCB cell. In terms of prediction, there is a 13.5% decrease in PCF, reducing it from 2.75 kN to 2.38 kN, while EA experiences a 7.8% increase, rising from 34.5 J to 37.2 J. In experimental results, PCF exhibits a 14% reduction, decreasing from 3.08 kN to 2.65 kN, while EA shows a 14.3% increase, climbing from 30.61 J to 35 J.

1. Introduction

The advent of automobiles has revolutionized transportation, but it has also brought with it the risk of traffic accidents, which pose a significant threat to people's safety and property. To address this issue, the installation of specially designed energy absorber is the main way to solve the crash problem[1] in traffic accident. Specifically, crash box is widely applied as energy absorption component, which is deployed in automobiles to protect passengers by dissipating the kinetic energy in a way of its deformation and fracture, also prevent front sub-frontal crash from crush damage.

Commonly, traditional crash boxes with simple cross-sections, such as squares, circles, and triangles, are often used due to their low cost and convenience of manufacturing[2-5]. However, installing traditional crash box will cause damage to passengers and goods due to their high initial peak force during impact, and their metal composition also increases the weight of the vehicle. To improve the energy absorption capability and reduce the initial peak force, researchers have introduced geometric imperfections into the design of crash boxes. Novel types of tubes have been developed with various triggers[6-10] to induce desired collapse modes, while emphasizing lightweight designs by utilizing the characteristics of fiber composite materials [11,12], which are lightweight and high in strength. In addition, researchers introduced rigid origami patterns as a geometric defect to improve energy absorption performance. For example, Ma J et al. [13] developed a new pre-folded crash box called the Origami Crash Box（OCB）, which features a collapse mode known as the complete diamond mode and has twice the number of traveling plastic hinge lines compared to a normal square tube. Experimental and theoretical studies have shown that the OCB outperforms the square tube in terms of average load while reducing the initial peak force [14]. Scholars have made a lot of efforts in structure optimization of the crash box with different methods. Ciampaglia A et al. [15] studied the impact response of OCB, which is made of carbon fiber/epoxy prepreg woven through experimental and simulation. Their study presented that the optimized OCB was provided with enhanced properties to the conventional OCB, and confirmed tune the geometry of OCB without affecting the mass would strengthen its attribute is possible. In advance, Zhang P et al. [16] discussed a pre-folded design that can guide the tube to achieve optimal energy dissipation by clustering analysis with a machine learning algorithm to identify key design parameters affecting energy consumption history. The result indicated that the OCB after they optimized shows a better energy absorption. In addition, Zhou C et al. [17] evaluated performance of mild steel OCB with different box geometry but in a stable area in 28800mm ^{2} and a thickness in 1mm under low velocity impact tests, in various of loading rates and tups, and three collapse modes was tested. Their experiments exhibited complete diamond model was sensitive to geometric imperfections, and it was the most efficient mode of energy absorption. Above all, although a lot of studies on OCB have been publish, an accurate model needs to be built in order to predict performance of different sizes OCB cell and design optimization for OCB cell is still a problem wait to be solved.

Low PCF and high SEA are crucial factors in the design of crash boxes. However, achieving both a high specific energy absorption and a low initial peak force simultaneously can be challenging. Therefore, a precise model should be developed to evaluate both initial peak force and SEA. Artificial Neural Network (ANN) models have been widely used to fit highly nonlinear relationships between inputs and outputs in various disciplines [18-20]. ANN always contains one input layer, several hidden layers and one output layer. In this paper, the ANN utilized which input layer contains three neurons, output layer contains one neuron, and two hidden layers to model the force change with the different size of crash box and displacement of quasi-static compression. In addition to the ANN model, Non-dominated Sorting Genetic Algorithm II (NSGA-II) [21] is chosen to solve this problem and find the Pareto set. NSGA-II is a multi-objective optimization algorithm that is commonly used to solve problems with multiple objectives [22-24]. It is able to efficiently identify a diverse set of Pareto optimal solutions, which can help designers make informed decisions about trade-offs between conflicting objectives.

This article is organized into six distinct chapters. The first chapter serves as the introduction, wherein a literature review is conducted. In the second chapter, mathematical model of OCB is elaborated upon, and the parameters that required to optimize is showed. Then in the third chapter, the empirical results of the conducted experiments are meticulously presented and analyzed. The fourth chapter, an ANN model is established to predict the non-linear relationships for the load force with the change of displacement. Proceeding to the fifth chapter, the optimization process is

undertaken utilizing the NSGA-II algorithm. Finally, the conclusion of this paper is presented, it offers a comprehensive wrap-up of study.

2. Mathematical model and structural parameters

The fundamental origami pattern for the OCB [25] is visually depicted in Fig. 1. In this graphical representation, the solid lines symbolize hill folds, while the dashed lines denote valley folds. When a thin sheet of material is progressively folded along these designated creases and subsequently joined at the opposite free edges, a novel tube configuration, referred as the origami crash box showed as Fig. 2. In order to optimize the structure of OCB cell, it is essential to identify the structural parameters of OCB. It is evident that l, b, and c play a pivotal role in defining the structural of the OCB model from unfolding diagram of OCB is illustrated in Fig. 1.

While maintaining a constant material weight, in order to determine l, b, and c, the OCB surface area fixed at 14400mm^2, a thickness at 1mm. And the configuration with $l = 60$mm, $b = 60$mm and $c = 30$mm is considered as the standard OCB. Then we can calculate l and b with $\frac{l}{b}$ so the first structure parameter showed as Eq. (1):

$$x_1 = \frac{l}{b} \tag{1}$$

Subsequently, the parameter c should be determined. It is obvious that the value of c has a relationship and other factors, particularly h and x, as evidenced in Fig. 3, where x represents the distance from the edge of the octagon to the edge of the quadrilateral as showed in Fig. 4. So, it is essential to calculate the value of x before calculate c, and x can be expressed as Eq. (2):
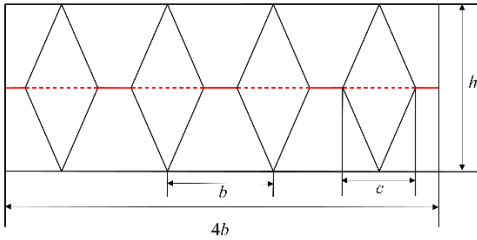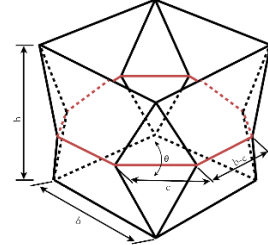

Figure 1: Unfolding diagram of OCB.
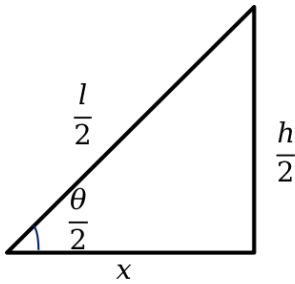

Figure 2: Structure of OCB cell.

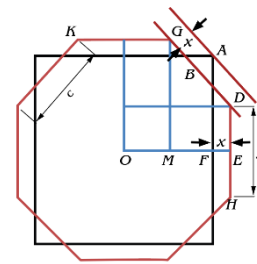Figure 3: Dihedral angle θ and its edges.

Figure 4: Top view of OCB.

$$x = FE = OE-OF = OM + ME-OF$$

$$= \frac{1}{2}KG + \frac{GD}{\sqrt{2}} - OF = \frac{b\text{-}c}{2} + \frac{c}{\sqrt{2}} - \frac{b}{2} = \frac{(\sqrt{2}-1)c}{2} \tag{2}$$

There is a relationship between dihedral angle θ and its edges showed in Fig. 3, and the relationship can be indicated as Eq. (3) and Eq. (4):

$$\cos\frac{\theta}{2} = \frac{2x}{l} = \frac{(\sqrt{2}\text{-}1)c}{l} \tag{3}$$

$$\sin\frac{\theta}{2} = \frac{h}{l} \tag{4}$$

The structure of OCB determines that θ is obtuse angle from Fig. 1, so $0 < \frac{\theta}{2} < \frac{\pi}{2}$ which means $0 < \cos\frac{\theta}{2} < 1$, with Eq. (3) the first constraint regarding c is obtained as $c < (\sqrt{2}+1)l$ and the second constraint is $c < b$ because the constraint of the OCB structure which can be deduced from the Fig. 1. Then the second parameter x_2 which will confirm c as Eq. (5) and $0 < x_2 < 1$:

$$x_2 = \frac{c}{\min((\sqrt{2}+1)l,\, b)} \tag{5}$$

Different $l,\ b$, and c will generate different h, so we formulate the maximum compression distance d as $0.6h$, and then we can get relationship between h and $l,\ c$ as showed as Eq. (6) and the third parameter s which is related with compression distance d as Eq. (7):

$$h = l\sin\frac{\arccos(\sqrt{2}-1)c}{l} \tag{6}$$

$$s = \frac{d}{0.6h} \tag{7}$$

Traditionally, the assessment of an OCB energy absorption capabilities during the crushing process relies on two key performance evaluation indicators: SEA and PCF. However, it is noteworthy that our OCB design prioritizes uniformity in weight across configurations. Therefore, in this context, EA is strategically employed as a paramount metric for measuring energy absorption performance. EA is expressed as Eq. (8), which $F(s)$ is the force that will change with the variation of s during crushing.

$$EA = 0.6h \int_0^1 F(s)ds \tag{8}$$

3. Experimental work

In this paper, we utilized the Ultimaker 2+ Connect as 3D printer and employed PATH-CF15, a type of carbon fiber nylon 3D printing material with a diameter of 2.85mm, to fabricate OCBs of varying sizes. The dimensions of the OCBs under investigation are intrinsically linked to the parameters x_1 and x_2. Therefore, it is imperative to precisely define the permissible ranges for these parameters. Accordingly, we specified the range for x_1 as $0.4 \le x_1 \le 1.2$ and for x_2 as $0.2 \le x_2 \le 0.8$, which contains the standard OCB size of $x_1 = 1$, and x_2 equals 0.5. To create a representative set of samples, 12 samples selected with pyDOE using Latin hypercube sampling, which is efficiently covers the sample space with a reduced number of samples, the result is illustrated as Fig. 5. As demonstrated in the Table 1, the sample configurations are presented in detail, the numbers refer to the identification assigned to each sample.

To assess the crashworthiness of the OCB cell, quasi-static testing technique is adopted. To conduct these tests effectively, the AGS-X (manufactured by Shimadzu Instruments Co., Ltd.) is utilized, which has the capability to sustain a complete load spectrum of up to 10kN to finished experiment. In quasi-static testing approach, we conducted the experiments at a controlled speed of 5mm/min, as illustrated in Fig. 6. The deformation history of the OCB cell during quasi-static testing is depicted in Fig. 7. It is able to be observed that diamond folded lobe concave inward with the increase of s, and the indenter will stop the experiment when s equals 1. To ensure the repeatability of the experiments and the accuracy of the data, every OCB cell configuration will be tested 5 times, and the force-displacement curve with the highest repeatability will be selected.
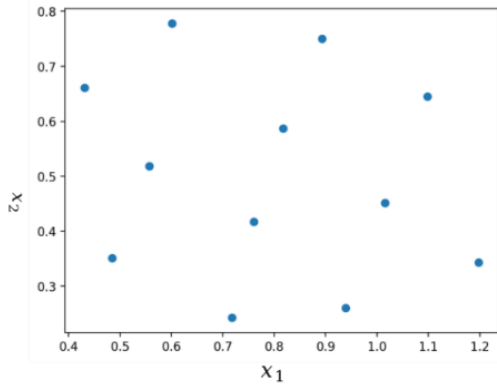
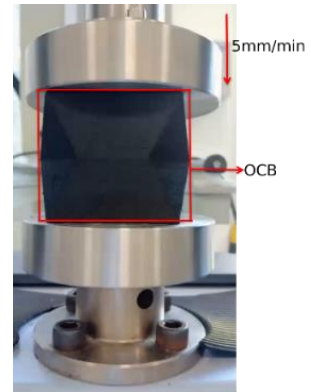Figure 5: Latin Hypercube Sampling Distribution

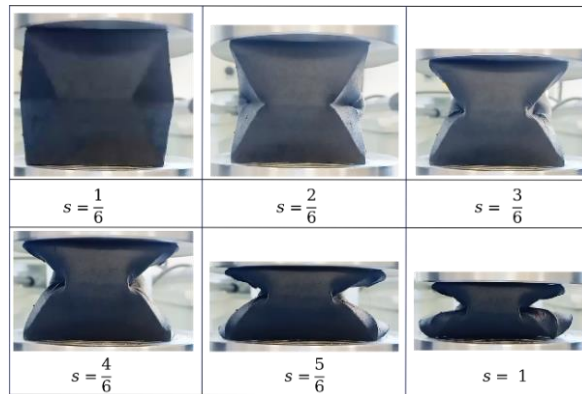Figure 6: Quasi-static testing of OCB cell

Figure 7: Deformation history of OCB cell (x_1=1.10, x_2=0.64)

Table 1: Result of Latin hypercube sampling

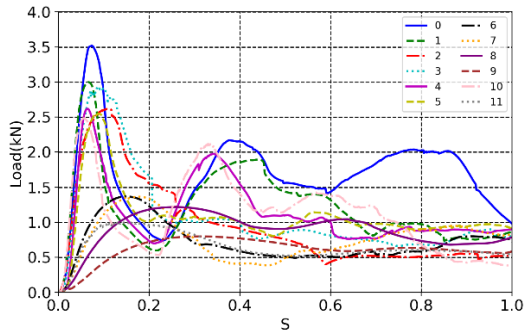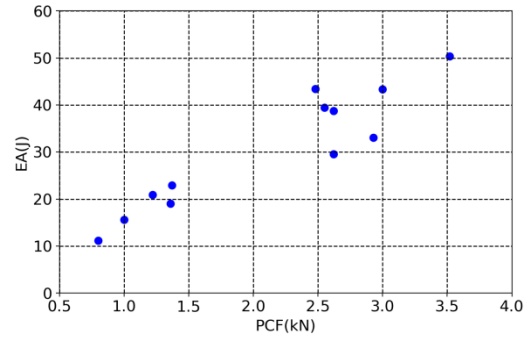| Number	x_1	x_2	l (mm)	b (mm)	c (mm)
0	0.72	0.24	50.8	70.8	17.2
1	1.02	0.45	60.5	59.5	26.9
2	0.82	0.59	54.2	66.4	38.9
3	0.76	0.42	52.3	68.8	28.7
4	0.94	0.26	58.1	61.9	16.1
5	1.10	0.64	62.9	57.3	36.9
6	0.89	0.75	56.7	63.5	47.6
7	0.56	0.52	44.8	80.4	41.6
8	0.60	0.78	46.5	77.4	60.2
9	0.43	0.66	39.4	91.4	60.4
10	1.20	0.34	65.7	54.8	18.8
11	0.49	0.35	41.8	86.1	30.2

Figure 8: The load-s curve of samples　　　Figure 9: The relationship between PCF and EA

The detailed parameters associated with the study are comprehensively presented in Tab 1. The primary objective of this investigation is to ensure consistency in the weight of OCB cell specimens. An examination of the tested OCB specimens, as depicted in Fig. 8. The highest energy absorption, totaling 50.4 J, is achieved at the configuration $x_1 = 0.72$ and $x_2 = 0.24$. Remarkably, this same configuration also generates the highest initial peak crush force, reaching 3.52 kN. Conversely, the lowest energy absorption, amounting to 11.18 J, is realized at the configuration $x_1 = 0.72$ and $x_2 = 0.24$. Notably, this configuration also yields the lowest initial peak crush force, registering at 0.8 kN. Fig. 9 visually elucidates the relationship between Predicted PCF and EA. The depicted relationship exhibits an approximate linearity, indicating that higher energy absorption corresponds to higher initial peak crush force. Consequently, the core focus of our research endeavor is centered on enhancing the energy absorption characteristics while concurrently mitigating the initial peak crush force of OCB cell.

4. Establishment of ANN model to predict load-s curve

Artificial neural networks (ANNs) serve as a robust mathematical model renowned for their capacity to perform highly effective nonlinear approximation. Prior to commencing the training process of an ANN model, it is imperative to partition the dataset into training dataset and validation dataset. In this study, a dataset comprising 12 load-s curves are sampled at approximately 1000 equidistant points. This results in a comprehensive dataset, consisting of 12,225 data sets, each encompassing specific inputs: x_1, x_2 and s, alongside the corresponding output, which represents load capacity. Equidistant sampling was performed from the 12 load-s curves to create the dataset. To ensure robust model training and assessment, 80% of the dataset is designated as the training set, while the remaining 20% serves as the validation set. MSE metric is employed to evaluate the performance of the ANN model. During the training process, the training dataset is leveraged to train the ANN using the gradient descent algorithm. Meanwhile, the MSE computed on the validation dataset is utilized to assess the structural soundness of the ANN model. The architecture of an ANN has a significant impact on the performance of the ANN. Specifically, it encompasses critical attributes such as the number of hidden layers and the quantity of nodes within each hidden layer. In this study, a comprehensive exploration of architectural configurations is conducted, encompassing single, dual, and triple hidden layers, with node counts ranging from 10 to 50. The configurations of activation function include two different activation functions which are ReLu (Rectified Linear Unit) and Sigmoid, those two functions illustrated in Fig. 10.
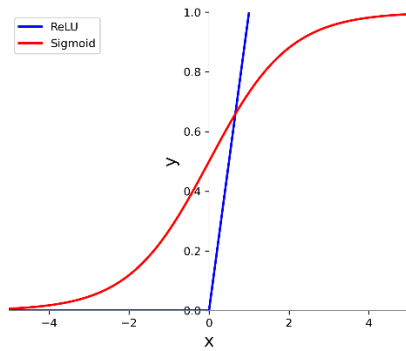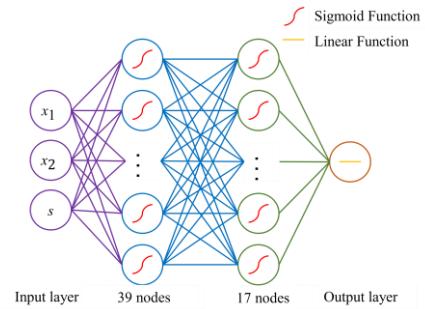
Figure 10: ReLu and Sigmoid

Figure 11: Best architecture of ANN

The ANN is systematically trained under various configurations using a fixed training set. The training parameters are consistently set to a batch size of 64, 100 training epochs, and the utilization of the Adam[26] optimizer with a learning rate of 0.1. These configurations are implemented in the TensorFlow[27]. The performance of the ANN models is rigorously assessed using the MSE computed on the validation dataset. This metric serves as a key indicator to evaluate the effectiveness and suitability of each ANN configuration. MSE of validation dataset is applied to assess the property of ANN. Through a comprehensive evaluation process, the architecture that excels with a validation set MSE of 0.021 kN^2 is identified as the best-performing configuration. This superior architecture encompasses two hidden layers, with the first hidden layer comprising 37 nodes and the second hidden layer comprising 19 nodes. Additionally, the Sigmoid activation function is applied to the hidden layers to facilitate their functionality. The architectural details are visually depicted in Figure 11.
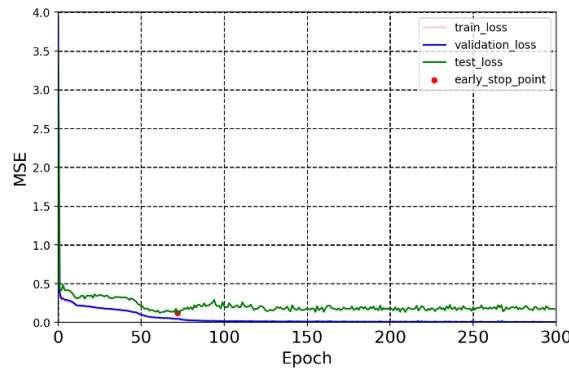

Figure 12: MSE of training dataset, validation dataset and test dataset over epochs
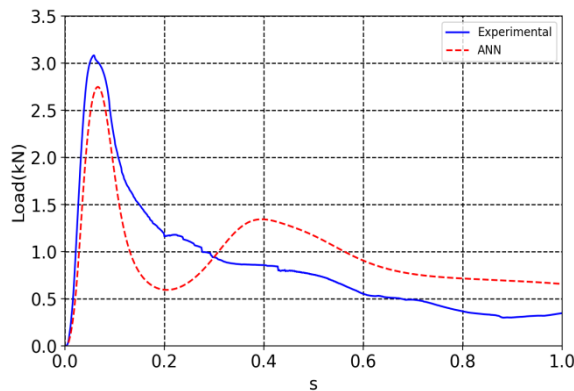

Figure 13: Load-s curve of experiment and ANN for test data

Subsequently, the training dataset is employed to train ANN using the optimal architecture. To safeguard against overfitting during the ANN training process, the experimental dataset of standard OCB cell (x_1=1, x_2=0.5) is utilized as test dataset. The training process, as illustrated in Fig. 12, reveals a consistent decrease in the MSE for both the training and validation datasets. However, From Figure 12, it is evident that the Mean Squared Error (MSE) for both the training and validation datasets exhibits a consistent decrease throughout the training process. However, the MSE for the test dataset demonstrates an initial decline, then increase after the 72th epoch as highlighted by the red point and finally enter a stable phase. Hence, an early stop at the 72th epoch is deemed essential to prevent overfitting of the ANN to the training dataset. And the ANN gets a MSE as 0.172kN^2 on test dataset, the result of ANN prediction and experiment is presented as Fig. 13.
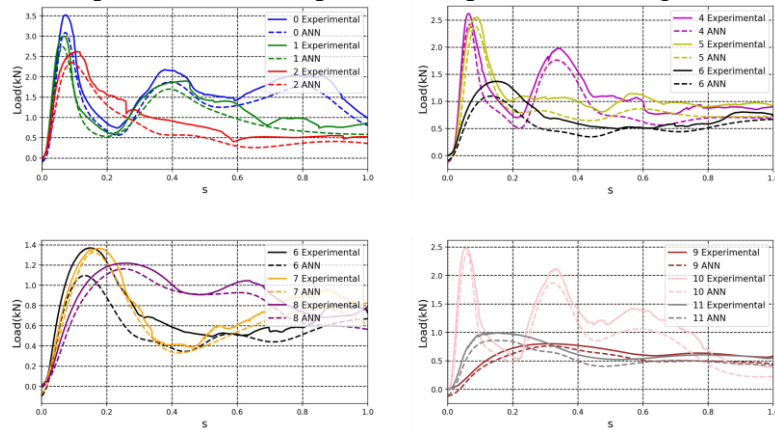

Figure 14: Load-s curves of experiment versus prediction of 12 samples

The experimental crushing behavior of samples versus the prediction of crushing behavior is illustrated at Fig. 14. Moreover, the result from Table 2 reveals that the largest disparity of PCF observed experimental results and ANN predictions amounts to 19.9%. Furthermore, the maximum discrepancy of EA between experimental values and ANN predictions stands at 27.5%. Additionally, the average of MSE of samples is 0.046 kN^2. In contrast, the MSE associated with the ANN predictions on the test dataset records 0.172 kN^2, with an EA error rate of 11.3% and a PCF error rate of 10.7%.

Table 2: EA, PCF of experiment compared with prediction of ANN and MSE of ANN

Number	$EA_{experiment}$ (J)	$EA_{predict}$ (J)	$PCF_{experiment}$ (kN)	$PCF_{predict}$ (kN)	MSE (kN^2)
0	50.38	42.20	3.52	3.08	0.081
1	43.37	35.75	3.00	2.73	0.053
2	29.53	22.38	2.62	2.34	0.061
3	33.09	23.98	2.93	2.86	0.096
4	38.73	30.79	2.62	2.42	0.058
5	39.47	31.13	2.55	2.38	0.057
6	22.94	19.83	1.37	1.10	0.035
7	19.02	16.46	1.36	1.32	0.013
8	20.90	18.93	1.22	1.16	0.009
9	11.18	9.49	0.80	0.76	0.009
10	43.45	34.30	2.48	2.38	0.062
11	15.59	12.78	1.00	0.89	0.015
test	30.61	34.50	3.08	2.75	0.172

5. Optimization based on NSGA-II

In contrast to single-objective optimization problems, which yield a single optimal solution, multi-objective optimization problems produce a set of solutions known as the Pareto optimal set. This set represents solutions that strike a balance among conflicting objectives, offering a spectrum of trade-off solutions. To address multi-objective optimization challenges, a range of Multi-Objective Evolutionary Algorithms (MOEAs) has been introduced and extensively studied in the literature [28]. These algorithms aim to obtain Pareto-optimal solutions that cater to multiple objectives. Among the various MOEAs available, NSGA-II (Non-dominated Sorting Genetic Algorithm II) [21] stands out as one of the most potent and widely used approaches. It is renowned for its effectiveness and ease of implementation. NSGA-II builds upon the foundation of NSGA (Non-dominated Sorting Genetic Algorithm) [29] and integrates the principles of genetic algorithms and non-dominated sorting. In this research, we employ NSGA-II to address a multi-objective optimization problem defined as follows:

$$\begin{cases} \text{Min} \quad PCF \\ \text{Max} \quad EA \\ \text{s.t.} \quad 0.4 \leq x_1 \leq 1.2 \\ \qquad 0.2 \leq x_2 \leq 0.8 \\ \qquad l \times b = 3600 \text{mm}^2 \end{cases} \tag{9}$$

In which EA and PCF can be calculated with two dimensionless parameters x_1, x_2 and ANN model. NSGA-II is complied with Pymoo[30], a concise description of the algorithm is provided below:

(1) Generate an initial population, denoted as P_0, with a total size of N.

(2) Generate an offspring population, denoted as Q_t, using a binary tournament selection process that relies on a crowding-comparison operator, as well as applying crossover and mutation operations on the parent population P_t, the subscript t signifies the generation number. The offspring population Q_t is subsequently merged with its parent population P_t to form the complete population R_t.

(3) The fast nondominated sorting approach is executed on entire population R_t to identify various nondominated fronts as F_1, F_2, etc.

(4) Form a new parent population P_{t+1} with a size of N by selecting individuals from the obtained fronts F_i.

(5) The above process is repeated until the maximum of iterations is attained.

Within this research endeavor, specific experimental settings are defined. The initial population size, denoted as N is established at a value of 30. Furthermore, the offspring population size is meticulously configured to accommodate 50 individuals. Lastly, the maximum number of iterations for the optimization process is capped at 100. The outcomes of the Pareto set are visually portrayed in Fig. 15, providing a comprehensive representation of the solutions achieved through the NSGA-II algorithm. Fig. 16 furnishes a detailed depiction of the Hypervolume metric over the course of the optimization process. Notably, it reveals the progression of the Hypervolume as it reaches a plateau phase after 86 iterations, achieving a maximum value of 0.76. This phenomenon signifies the convergence of the NSGA-II algorithm towards an optimal solution set.
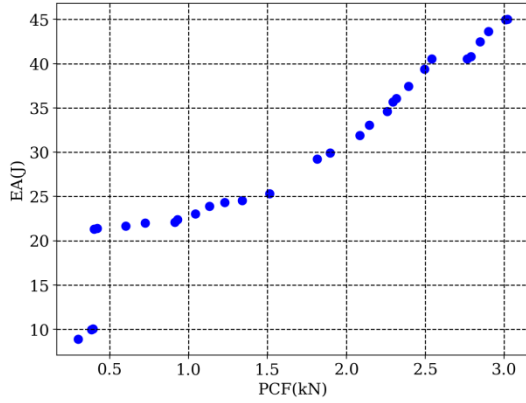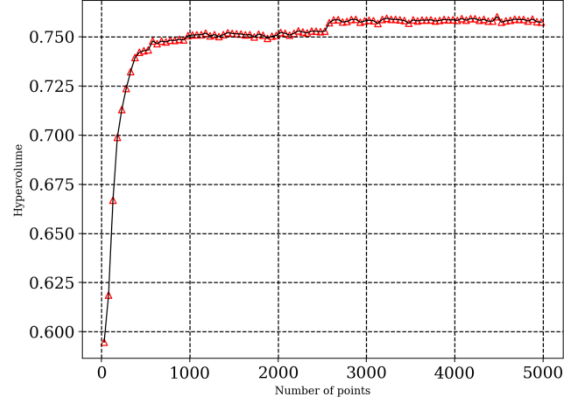
Figure 15: Pareto set of NSGA-II

Figure 16: Hypervolume

In order to assess the trustworthiness of Pareto set, a representative sample which shows a better performance than standard OCB box with the configuration x_1=1.20, x_2=0.63 is selected. This specific sample is chosen for a detailed comparative analysis between experimental and predictive outcomes, the results of which are elucidated in Fig. 17. The predictive outcomes for this selected sample are as follows:

(1) The PCF is estimated at 2.38 kN, exhibiting a relative error of 10.2% when contrasted with the experimental PCF value of 2.65 kN.

(2) The EA prediction yields a value of 37.2 J, demonstrating a relative error of 6.0% compared to the experimental EA value of 35.0 J.

Tab 3 shows the configurations of Pareto set and PCF, EA predicted by ANN. The results indicate that the highest EA value observed is 44.97J, corresponding to a configuration with x_1=0.72, x_2=0.20. Conversely, the lowest PCF value recorded is 0.3 kN, associated with a configuration with x_1=0.4, x_2=0.52.

Table 3: Parameters, PCF and EA of ANN prediction for Pareto set

x_1	x_2	PCF (kN)	EA(J)
0.40	0.52	0.30	8.91
0.72	0.20	3.03	44.97
0.82	0.80	0.92	21.45
0.44	0.51	0.38	9.91
1.20	0.20	1.81	29.22
0.99	0.80	1.51	25.28
1.20	0.72	2.09	32.00
1.20	0.22	1.91	30.02
1.20	0.52	2.54	40.53
0.80	0.74	0.61	21.42
0.77	0.71	0.93	22.38
0.76	0.20	2.85	42.62
0.78	0.20	2.75	40.16
1.20	0.70	2.15	33.16
0.71	0.71	1.34	24.55
0.75	0.68	0.99	22.73
0.71	0.75	1.23	24.25
0.75	0.20	2.90	43.70
0.77	0.71	0.93	22.38

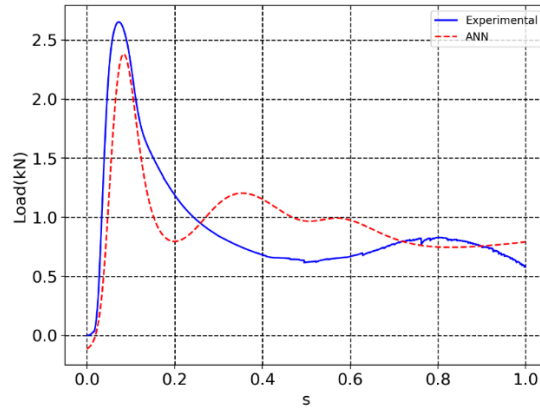|			
1.20	0.65	2.32	36.12
0.77	0.21	2.82	41.28
1.20	0.63	2.38	37.20
0.82	0.79	0.44	21.33
0.73	0.20	2.99	44.88
1.20	0.58	2.49	39.38
1.19	0.67	2.26	34.44
0.77	0.72	0.94	22.61
0.73	0.80	1.13	23.92
1.20	0.66	2.29	35.53
0.44	0.51	0.38	9.91

Figure 17: Experimental and predicted Load-s curves with configuration x_1=1.20, x_2=0.63

6. Conclusion

In this paper, we have derived two crucial parameters x_1 and x_2, from mathematical model to precisely define the size of OCB cell in a stable surface and thickness. Then selecting 12 representative samples with Latin hypercube sampling, those samples have test with quasi-static testing in a speed of 5mm/min. The dataset contains 12255 points sample from 12 cures at equal intervals. In order to training ANN model, we divided the dataset into training and validation sets, allocating 80% for training and 20% for validation. ANN is trained with training dataset and MSE of validation dataset is used to evaluate its performance. The experimental data of standard OCB cell is utilized as test data to prevent overfitting during training with best architecture. After that, NSGA-II is applied to generate Pareto set based on ANN, and Hypervolume is used to evaluate the convergence of NSGA-II. To assess the trustworthiness of Pareto set, one solution is selected from Pareto set which dominates standard OCB cell, and experiment has proved it. The main conclusions drown from this study are as follows:

1) A mathematical model is established of OCB cell and two crucial parameters x_1 and x_2 is defined to describe the OCB cell in a stable surface and thickness.

2) ANN model is built with a MSE of training data as 0.046kN^2, and MSE of test data as 0.172kN^2. With this ANN prediction, PCF of samples gets maximum error of 19.9%, and EA as 27.5%. Experiment shows that PCF of test data gets an error of 10.7% and EA as 11.3%.

3) One solution is selected shows a superior performance from Pareto set generated by NSGA-II than standard OCB. Prediction indicates that PCF reduce from 2.75 kN to 2.38 kN, representing a 13.5% reduction, while EA with an increase of 7.8%, rising from 34.5 J to 37.2 J. In experimental results, PCF demonstrates a 14% reduction, decreasing from 3.08 kN to 2.65 kN. Concurrently, EA

experiences a 14.3% increase, climbing from 30.61 J to 35 J.

4) The Pareto set indicate that the highest EA value observed is 44.97J, corresponding to a configuration with $x_1=0.72$, $x_2=0.20$. Conversely, the lowest PCF value recorded is 0.3 kN, associated with a configuration with $x_1=0.4$, $x_2=0.52$.

This paper applied ANN and NSGA-II to get a Pareto set, which provide some specific configurations of OCB cell for choosing.

References

[1] Olabi, A.-G., E. Morris, and M. Hashmi, *Metallic tube type energy absorbers: a synopsis. Thin-walled structures, 2007. 45(7-8): p. 706-726.*

[2] Hong, W., et al., *Quasi-static axial compression of triangular steel tubes. Thin-Walled Structures, 2013. 62: p. 10-17.*

[3] Jensen., M. Langseth, and O. Hopperstad, *Experimental investigations on the behaviour of short to long square aluminium tubes subjected to axial loading. International Journal of Impact Engineering, 2004. 30(8-9): p. 973-1003.*

[4] Guillow, S., G. Lu, and R. Grzebieta, *Quasi-static axial compression of thin-walled circular aluminium tubes. International Journal of Mechanical Sciences, 2001. 43(9): p. 2103-2123.*

[5] Abramowicz, W. and N. Jones, *Dynamic axial crushing of square tubes. International Journal of Impact Engineering, 1984. 2(2): p. 179-208.*

[6] Shakeri, M., R. Mirzaeifar, and S. Salehghaffari, *New insights into the collapsing of cylindrical thin-walled tubes under axial impact load. Proceedings of the Institution of Mechanical Engineers, Part C: Journal of Mechanical Engineering Science, 2007. 221(8): p. 869-885.*

[7] Lee, S., et al., *Effect of triggering on the energy absorption capacity of axially compressed aluminum tubes. Materials & design, 1999. 20(1): p. 31-40.*

[8] Gupta, N. and S. Gupta, *Effect of annealing, size and cut-outs on axial collapse behaviour of circular tubes. International journal of mechanical sciences, 1993. 35(7): p. 597-613.*

[9] Gupta, N., *Some aspects of axial collapse of cylindrical thin-walled tubes. Thin-walled structures, 1998. 32(1-3): p. 111-126.*

[10] Salehghaffari, S., et al., *Attempts to improve energy absorption characteristics of circular metal tubes subjected to axial loading. Thin-Walled Structures, 2010. 48(6): p. 379-390.*

[11] Zarei, H., M. Kröger, and H. Albertsen, *An experimental and numerical crashworthiness investigation of thermoplastic composite crash boxes. Composite structures, 2008. 85(3): p. 245-257.*

[12] Hussain, N.N., S.P. Regalla, and Y.V.D. Rao, *Low velocity impact characterization of glass fiber reinforced plastics for application of crash box. Materials Today: Proceedings, 2017. 4(2): p. 3252-3262.*

[13] Ma, J., *Thin-walled tubes with pre-folded origami patterns as energy absorption devices. 2011, University of Oxford.*

[14] Ma, J. and Z. You. *A novel origami crash box with varying profiles. in International Design Engineering Technical Conferences and Computers and Information in Engineering Conference. 2013. American Society of Mechanical Engineers.*

[15] Ciampaglia, A., et al., *Impact response of an origami-shaped composite crash box: Experimental analysis and numerical optimization. Composite Structures, 2021. 256: p. 113093.*

[16] Zhang, P., et al., *Performance Study of Origami Crash Tubes Based on Energy Dissipation History. Energies, 2022. 15(9): p. 3109.*

[17 Zhou, C., et al., *Dynamic axial crushing of origami crash boxes. International journal of mechanical sciences, 2016. 118: p. 1-12.*

[18] Dimiduk, D.M., E.A. Holm, and S.R. Niezgoda, *Perspectives on the impact of machine learning, deep learning, and artificial intelligence on materials, processes, and structures engineering. Integrating Materials and Manufacturing Innovation, 2018. 7: p. 157-172.*

[19] Ružiak, I., et al., *Artificial neural networks prediction of rubber mechanical properties in aged and nonaged state. Improved Performance of Materials: Design and Experimental Approaches, 2018: p. 27-35.*

[20] al-Swaidani, A.M. and W.T. Khwies, *Applicability of artificial neural networks to predict mechanical and permeability properties of volcanic scoria-based concrete. Advances in civil engineering, 2018. 2018.*

[21] Deb, K., et al., *A fast and elitist multiobjective genetic algorithm: NSGA-II. IEEE transactions on evolutionary computation, 2002. 6(2): p. 182-197.*

[22] Wang, S., et al., *The origami inspired optimization design to improve the crashworthiness of a multi-cell thin-walled structure for high speed train. International Journal of Mechanical Sciences, 2019. 159: p. 345-358.*

[23] Sun, G., et al., *Crashing analysis and multiobjective optimization for thin-walled structures with functionally graded thickness. International Journal of Impact Engineering, 2014. 64: p. 62-74.*

[24] Sheriff, N.M., et al., Optimization of thin conical frusta for impact energy absorption. Thin-Walled Structures, 2008. 46(6): p. 653-666.

[25] Ma, J. and Z. You, The origami crash box. Origami, 2011. 5: p. 277-290.

[26] Kingma, D.P. and J. Ba, Adam: A method for stochastic optimization. arXiv preprint arXiv:1412.6980, 2014.

[27] TensorFlow Developers. (2023). TensorFlow (v2.12.1). Zenodo. https://doi.org/10.5281/zenodo.8118033.

[28] Marler, R.T. and J.S. Arora, Survey of multi-objective optimization methods for engineering. Structural and multidisciplinary optimization, 2004. 26: p. 369-395.

[29] Srinivas, N. and K. Deb, Muiltiobjective optimization using nondominated sorting in genetic algorithms. Evolutionary computation, 1994. 2(3): p. 221-248.

[30] J. Blank and K. Deb, "Pymoo: Multi-Objective Optimization in Python," in IEEE Access, vol. 8, pp. 89497-89509, 2020, doi: 10.1109/ACCESS.2020.2990567.